A Multiple Hypothesis Based Method for Particle Tracking and Its Extension for Cell Segmentation*

Liang Liang, Hongying Shen, Panteleimon Rompolas, Valentina Greco, Pietro De Camilli, and James S. Duncan

Yale University, New Haven, CT 06520, USA
liang.liang@yale.edu

Abstract. In biological studies, it is often required to track thousands of small particles in microscopic images to analyze underlying mechanisms of cellular and subcellular processes which may lead to better understanding of some disease processes. In this paper, we present an automatic particle tracking method and apply it for analyzing an essential subcellular process, namely clathrin mediated endocytosis using total internal reflection microscopy. Particles are detected by using image filters and subsequently Gaussian mixture models are fitted to achieve sub-pixel resolution. A multiple hypothesis based framework is designed to solve data association problems and handle splitting/merging events. The tracking method is demonstrated on synthetic data under different scenarios and applied to real data. We also show that, by equipping with a cell detection module, the method can be extended straightforwardly for segmenting cell images taken by two-photon excitation microscopy.

1 Introduction

With the rapid development in fluorescence microscopy, biologists can observe the dynamics of individual particles and investigate the underlying mechanisms of cellular processes which may reveal mechanisms of some disease processes. We are particularly interested in clathrin mediated endocytosis (CME). CME [1] is an essential cellular process that cells use to take up nutrients, to internalize plasma membrane proteins, and to recycle lipid components on the plasma membrane. The process consists of several stages [1] as illustrated in Fig. 1: clathrin coat assembly, clathrin coat maturation, clathrin coated pits (CCPs) fission into clathrin coated vesicles, and finally vesicles uncoating clathrin. CCP intensity increases as it grows up, and remains relatively stable when it matures, and decreases when it releases its coat. CCP motion is a kind of constrained Brownian motion.

The study of this process has profound implications in neuroscience and virology. For instance, CME is the major route for synaptic vesicle recycling in neurons critical for synaptic transmission [1], and dysfunction of the process may be the symptom of certain disease [1]. It is also one of the pathways through

* This work was supported in part by the Keck Foundation.

J.C. Gee et al. (Eds.): IPMI 2013, LNCS 7917, pp. 98–109, 2013.

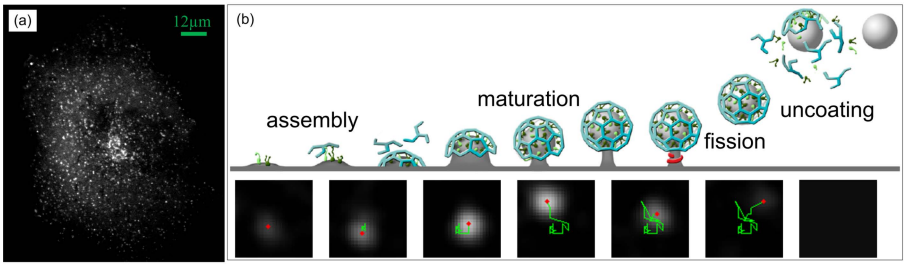

Fig. 1. (a) A Cell image. (b) Different stages of CME, and an image sequence (smoothed) showing a CCP in different stages. Clathrin is fluorescently labeled. The red dots indicate the center positions and the green lines represent the trajectories.

which viruses enter cells [2]. Since typical image datasets from an experiment consist of several thousand image frames, manual processing is almost infeasible. In the literature, there are some particle tracking methods for different biological applications [3,4,5]. For example, in [3], a method is presented to track quantum dots which can rapidly switch between acceleration mode and steady speed mode which are described by multiple motion models. Since the properties of CCPs are different from those particles, those methods are not directly applicable for our application. Due to the importance and complexity of CME, it is worth developing a method for CCP tracking.

Tracking frameworks are also essential for managing multiple trajectories. Most of the particle tracking methods in literature consider tracking as a MAP (maximum a posteriori) problem, and try to solve it in various ways. Some methods use stochastic sampling based frameworks, e.g., particle filter [6] to explore the probability space of the trajectories spatially and temporally when the tracking problem is nonlinear and non-Gaussian. Many other methods are based on the classical multiple hypothesis tracking (MHT) framework [7] and its variants [8,9,4,3]. In the MHT framework, particle tracking can be decomposed to three sub-tasks: particle detection, particle state estimation and prediction, and linking between established trajectories and newly detected particle locations. The known issue of the MHT framework is the solution space will expand exponentially fast, and many methods [10] have been proposed to overcome the issue. The results from MHT based methods are strictly reproducible compared to the stochastic approach, and therefore we choose MHT as the base framework.

The MHT framework has an implicit assumption that the observations of the targets are already given by the detection module, except that it is not known which observation corresponds to which target and vise versa. The assumption can be violated if the observations are imperfect. splitting and merging events occur frequently in our application. For example, some CCPs may temporarily crowd together and then move apart. As a result, there are many suspicious observations obtained by the detection module, each of which may correspond to several particles, and the number of the corresponding real particles and their states are all unknowns. A method in [11] uses k-means based functions to cut

the suspicious observations to pieces, and find the best result. That concept is not applicable for our application because the local intensity profile of the crowded particles is a mixture of Gaussian functions, and small spatial segments of the profile are meaningless. Another method in [12] tries to fit more than one Gaussian functions around each suspicious observation. Since the number of the real particles is unknown, and the goodness of fitting will increase as the number of the Gaussian functions increases, the optimal number of Gaussian functions can not be determined.

In this paper, we present an extended version of the classical MHT framework. Since it considers more types of hypotheses, it can handle the splitting/merging events effectively without user intervention, and prevent independent CCP trajectories from linking together. The models used in the paper are based on our previous works [13]. The proposed method is quantitatively evaluated on synthetic image datasets and it is also applied to real data. The method is not limited for CCP analysis only, and we show that by using an ellipse-shaped cell detection module, the method can be used for cell segmentation.

2 Tracking Framework

In this section, we describe the general framework including hypothesis generation and optimization by integer programming. In section 3, we will show how to apply the framework for CCP tracking.

2.1 The Extended MHT Framework

Let $\mathbf{I}_t$ be the image taken at time t (frame index). Let $\mathbf{X}_t$ be the joint state of all targets (i.e., particles) at time t, assembled from each target's state $X_t^{(k)}$. Let $\mathbf{D}_t$ be the observation set, and $D_t^{(j(k,t))}$ be the observation of the target k at time t. The goal is to find the target states $\{\widehat{\mathbf{X}}_t\}_{t=1}^{t_{max}}$ that maximize the posterior probability (MAP) given the dataset $\{\mathbf{I}_t\}_{t=1}^{t_{max}}$, i.e., maximize the energy $\mathbf{E}$:

$$\mathbf{E} = \log p\left(\{\mathbf{X}_t\}_{t=1}^{t_{max}} \left| \{\mathbf{I}_t\}_{t=1}^{t_{max}}\right.\right) \tag{1}$$

Here, $\{\mathbf{X}_t\}_{t=1}^{t_{max}} = \{\mathbf{X}_1, ..., \mathbf{X}_{t_{max}}\}$. Since it is difficult to find the optimal solution directly, we try to maximize the lower bound $\widehat{\mathbf{E}}$ of the above energy. Assuming the targets are statistically independent of each other, then we obtain

$$\widehat{\mathbf{E}} = \sum_k \alpha^{(k)} E_P^{(k)} + \sum_t E_{I_t} \tag{2}$$

$$E_P^{(k)} = \log p\left(\{X_t^{(k)}\}_{t=1}^{t_{max}}\right) + \sum_t \log p\left(D_t^{(j(k,t))} \left| X_t^{(k)}\right.\right) \tag{3}$$

$$E_{I_t} = \log p\left(\mathbf{I}_t \left| \mathbf{D}_t\right.\right) \tag{4}$$

Each target trajectory $\{X_t^{(k)}\}_{t=1}^{t_{max}}$ is a hypothesis and has an indicator $\alpha^{(k)} \in \{0, 1\}$. If $\alpha^{(k)} = 1$, the trajectory k is selected as a real trajectory, and if $\alpha^{(k)} = 0$,

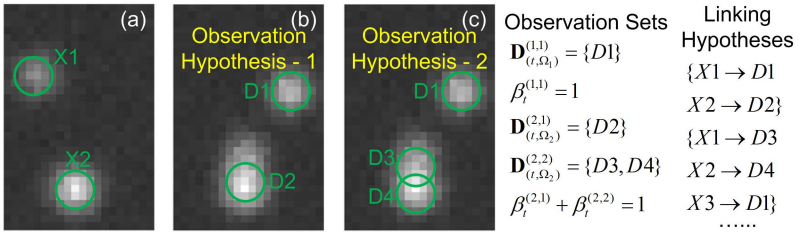

Fig. 2. (a) Two particles in time t-1. (b) Two observations at time t. (c) Three observations at time t.

it is discarded as a false trajectory. By considering different correspondences between the target tags and the observations, multiple trajectory hypotheses can be generated. One to one correspondence is assumed, which is the constraint of the maximization problem.

If we only use the above equations as the framework, then it will just be the classical MHT. We further extend the framework by considering multiple observation hypotheses. In most cases, each image $\mathbf{I}_t$ can be segmented into small regions $\{\Omega_m\}_{m=1}^{m_{max}}$. Each sub-image $\mathbf{I}_{(t,\Omega_m)}$ contains one ore more observations. In each image region, we find many observation sets, and each set of them, $\mathbf{D}^{(m,n)}_{(t,\Omega_m)}$ indexed by n, can describe the sub-image independently. Therefore, we extend the Eq.(4) to

$$E_{I_t} = \sum_m \sum_n \beta_t^{(m,n)} E_{I_t}^{(m,n)} \tag{5}$$

$$E_{I_t}^{(m,n)} = \log p\left(\mathbf{I}_{(t,\Omega_m)} \middle| \mathbf{D}^{(m,n)}_{(t,\Omega_m)}\right) \tag{6}$$

$$\sum_n \beta_t^{(m,n)} = 1, \; and \; \beta_t^{(m,n)} \in \{0,1\} \tag{7}$$

Each observation set $\mathbf{D}^{(m,n)}_{(t,\Omega_m)}$ is a hypothesis and has an indicator $\beta_t^{(m,n)} \in \{0,1\}$. If $\beta_t^{(m,n)} = 1$, the observation set is selected as real observation, and if $\beta_t^{(m,n)} = 0$, then it is false. Each single observation in the set also has an indicator equal to $\beta_t^{(m,n)}$. If there is only one observation in the set, then its indicator is 1. The method for generating observation sets is not defined here, we leave it to be implemented in different applications. By generating multiple observation hypotheses and finding the best hypothesis, the problem caused by splitting/merging can be solved. Fig. 2 shows the observation hypotheses generated in a simple scenario.

2.2 Solving the Optimization Problem

After obtaining the hypotheses of trajectories and observations, the only task left is to find the set of hypotheses as a solution that is feasible and maximizes

the energy in Eq.(1). In a feasible solution, there must not exist any observation which is shared by more than one trajectories, and there must not exist any pair of observation sets, each of which explains the same image region. The feasibility definition is used to ensure one to one correspondences. Eq.(2) and its constraints can be rewritten to the matrix forms, given by

$$maximize : \widehat{\mathbf{E}} = E'\boldsymbol{\gamma} \tag{8}$$

$$subject\ to : \mathbf{A}\boldsymbol{\alpha} = \widetilde{\boldsymbol{\beta}} \tag{9}$$

$$\mathbf{B}\boldsymbol{\beta} = \mathbf{1} \tag{10}$$

After integer programming is applied, the solution is obtained as a binary vector $\boldsymbol{\gamma}$ defined as $\boldsymbol{\gamma} = [\boldsymbol{\alpha}, \boldsymbol{\beta}]'$. $\boldsymbol{\alpha}$ and $\boldsymbol{\beta}$ are two binary vectors assembled from every unknown $\alpha^{(k)}$ and every unknown $\beta_t^{(m,n)}$ respectively. $\widetilde{\boldsymbol{\beta}}$ is a vector assembled from all the observation indicators, and therefore its length equals to the total number of individual observations. We note that some of the observation indicators are known as 1. E is a vector assembled from all the corresponding $E_P^{(k)}$and $E_{I_t}^{(m,n)}$. $\mathbf{A}$ is a sparse binary matrix. Only if the trajectory k has the observation indexed by l, then $\mathbf{A}(l,k) = 1$. The summation of the indicators of the trajectories that have the same observation (e.g., the one indexed by l) is equal to the indicator of the observation, which is the one-to-one mapping constraint described by Eq.(9). $\mathbf{B}$ is a sparse binary matrix. $\mathbf{1}$ is a vector and all its elements are equal to 1. Eq.(10) is just the matrix form of Eq.(7).

3 Tracking Clathrin Coated Pits in 2D+t

3.1 State Space Models and Filters

We assume particle dynamics can be modeled using linear state space models [14] with a certain probability distribution at each time. Each model is given as

$$X_t^{(k)} = F_t^{(i)} X_{t-1}^{(k)} + U_t^{(i,k)} + W_t^{(i)} \tag{11}$$

$$D_t^{(j(k,t))} = H X_t^{(k)} + V_t^{(j(k,t))} \tag{12}$$

Here, $F_t^{(k)}$ is the state transition matrix. $U_t^{(i,k)}$ is the external input. $W_t^{(i)}$ is the process noise with covariance matrix $Q_t^{(i)}$. H is a constant observation matrix. $V_t^{(j(k,t))}$ is the observation noise with covariance matrix $R_t^{(j(k,t))}$. Each of these noise sources is assumed to be Gaussian and independent. The model parameters can be estimated from training data.

We define the state of particle k at time t as $X_t^{(k)} = [x_t^{(k)}, y_t^{(k)}, a_t^{(k)}, \dot{a}_t^{(k)}, r_t^{(k)}]'$. $[x_t^{(k)}, y_t^{(k)}]$ is its position. $a_t^{(k)}$ is its intensity, and $\dot{a}_t^{(k)}$ is the rate of intensity change over time. $r_t^{(k)}$ is its relative radius. We use two linear state space models. For particle motion, the first model describes it as free Brownian motion, and the second model describes it as confined motion because each particle is linked to the plasma membrane through its neck and can only move within a restricted

region until the fission stage [1]. For intensity variation, both models describe it as a linear process. The matrices are given by

$$F_t^{(1)}=\begin{bmatrix}1&0&0&0&0\\0&1&0&0&0\\0&0&1&1&0\\0&0&0&1&0\\0&0&0&0&1\end{bmatrix},\ F_t^{(2)}=\begin{bmatrix}0&0&0&0&0\\0&0&0&0&0\\0&0&1&1&0\\0&0&0&1&0\\0&0&0&0&1\end{bmatrix},U_t^{(2,k)}=\begin{bmatrix}\bar{x}_{t-1}^{(k)}\\ \bar{y}_{t-1}^{(k)}\\0\\0\\0\end{bmatrix},\ H=\begin{bmatrix}1&0&0&0&0\\0&1&0&0&0\\0&0&1&0&0\\0&0&0&0&1\end{bmatrix}$$

$U_t^{(1,k)}$ is a zero vector, and $U_t^{(2,k)}$ is the force that keeps the particle staying near its neck joint which is estimated by the time-average position $[\bar{x}_t^{(k)}, \bar{y}_t^{(k)}]$. $\bar{x}_t^{(k)} = \frac{1}{t-t_1+1}\sum_{\tau=t_1}^{t} x_\tau^{(k)}$, and t_1 is the time the particle appears. Also, let t_2 be the time the particle disappears. Then the particle lifetime is $t_2 - t_1 + 1$.

Since the process is assumed to be Markovian, we obtain

$$p\left(\{X_t^{(k)}\}_{t=1}^{t_{max}}\right) = p\left(X_1^{(k)}\right)\prod_{t=2}^{t_{max}} p\left(X_t^{(k)}|X_{t-1}^{(k)}\right) \tag{13}$$

To deal with appearing/disappearing, we set $X_{t_1-1}^{(k)} = [x_{t_1}^{(k)} + 0.707\Delta, y_{t_1}^{(k)} + 0.707\Delta, 0, \dot{a}_{t_1}^{(k)}, r_{t_1}^{(k)}]'$ and $X_{t_2+1}^{(k)} = [x_{t_2}^{(k)} + 0.707\Delta, y_{t_2}^{(k)} + 0.707\Delta, 0, \dot{a}_{t_2}^{(k)}, r_{t_2}^{(k)}]'$ where Δ is the maximum displacement. We define $p(X_t^{(k)}|X_{t-1}^{(k)}) = p(X_{t_1}^{(k)}|X_{t_1-1}^{(k)})$ for $t < t_1 - 1$ and $p(X_t^{(k)}|X_{t-1}^{(k)}) = p(X_{t_2+1}^{(k)}|X_{t_2}^{(k)})$ for $t > t_2 + 1$, which means the states are irrelevant before the particle is created and after it disappears.

The computation of $E_P^{(k)}$ is simplified. In the right side of Eq.(3), the second term can be ignored because observation noise level is much smaller than process noise level in our application. The element in Eq.(13) can be approximated as

$$\log p\left(X_t^{(k)}|X_{t-1}^{(k)}\right) \approx -\left\|H\left(X_t^{(k)} - \widetilde{X}_t^{(k)}\right)\right\|^2_{\widetilde{Q}_t^{(i^*)}} \tag{14}$$

Here, $\widetilde{X}_t^{(k)}$is the predicted state, and $\widetilde{Q}_t^{(i^*)} = HQ_t^{(i^*)}H'$ where i^* is the index of the most probable model at time t. The vector norm is defined as $\|X\|_Q^2 = X'Q^{-1}X$. We insert the H matrix in the norm to ensure that only observable features are used to evaluate the goodness of each trajectory.

For state estimation and prediction, we use the well known IMM filter [14,3]. In addition, the feasible range of the observation of a particle is also calculated, which is realized by using the gating technique [9].

3.2 Initial Detection

The fluorescence intensity in the 2D x-y plane can be well modeled using Gaussian mixtures, which is well studied in literature [5]. Before it is captured by the EMCCD camera, the 2D fluorescence image f_t can be modeled as the sum of Gaussian mixture G_t and background b_t, given by

$$f_t(x, y) = G_t(x, y) + b_t(x, y) \tag{15}$$

The Gaussian mixture G_t has multiple components, i.e., $G_t = \sum_j G_t^{(j)}$. Each component corresponds to a feature/observation vector $D_t^{(j)} = [x_t^{(j)}, y_t^{(j)}, a_t^{(j)}, r_t^{(j)}]$, given by

$$G_t^{(j)}(x,y) = a_t^{(j)} \exp\left[-\frac{(x-x_t^{(j)})^2 + (y-y_t^{(j)})^2}{2(r_t^{(j)})^2}\right] \tag{16}$$

The image $\mathbf{I}_t$ from the EMCCD camera is determined by the fluorescence image f_t and the noise sources [15], which can be approximated as

$$\mathbf{I}_t(x,y) \approx f_t(x,y) + N_t\left(0, \sigma^2_{(t,x,y)}\right) \tag{17}$$

$$\log p\left(\mathbf{I}_t \,|\mathbf{D}_t\right) \approx -\sum_{(x,y)} \frac{\left(f_t(x,y) - \mathbf{I}_t(x,y)\right)^2}{\sigma^2_{(t,x,y)}} \tag{18}$$

N_t is Gaussian noise with variance $\sigma^2_{(t,x,y)} = 2\left(G_t(x,y) + b_t(x,y)\right)$ and zero-mean. The approximation is only used for feature estimation not for simulation.

According to the above analysis, we have developed a detection method [16]. Initial positions of the particles are identified in each image by using matched filters. Then, image background is estimated and Gaussian mixture models are fitted to obtain the full observation vectors. By thresholding the filtered images, each image is segmented into regions containing particles.

3.3 Multiple Hypothesis Generation

We use four types of trajectory hypotheses: initiation/appearing, extension, termination, and breaking. Let's assume that trajectories (hypotheses) up to time $t-1$ and observations at time t have been obtained. The first three can be made straightforwardly. A hypothesis of trajectory breaking is made, if the intensity curve of an established trajectory has more than two local minima. The breaking points are at the local minima. This hypothesis will help to prevent independent trajectories jointing together.

Since the initial detection may not be accurate, multiple observation hypotheses are generated. Let's suppose that trajectories up to time $t-1$ have been obtained. In the image $\mathbf{I}_t$, each segmented region Ω_m intersects the predicted observation regions of the particles $\{X^{(k_1)}, X^{(k_2)}, ...\}$. Then, for each subset $\{X^{(k_{h_1})}, X^{(k_{h_2})}, ...\}$ of the particles, we can find their observation set $\mathbf{D}^{(m,n)}_{(t,\Omega_m)}$ which maximizes the energy:

$$E_O^{(m,n)} = \log p\left(\mathbf{I}_{(t,\Omega_m)} \left| \mathbf{D}^{(m,n)}_{(t,\Omega_m)}\right.\right) - \lambda_a \sum_h \left(a_t^{(k_h)} - \widetilde{a}_t^{(k_h)}\right)^2 \tag{19}$$

subject to (for each k_h)

$$\left(x_t^{(k_h)} - \widetilde{x}_t^{(k_h)}\right)^2 + \left(y_t^{(k_h)} - \widetilde{y}_t^{(k_h)}\right)^2 < \triangle^2 \tag{20}$$

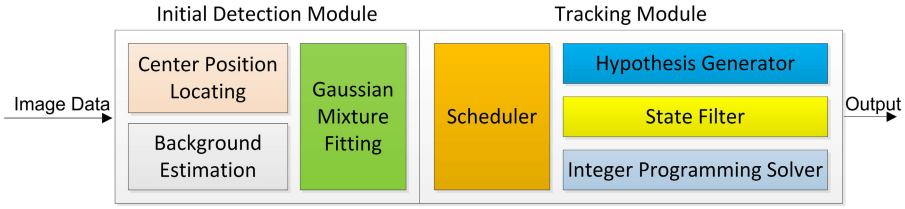

Fig. 3. The diagram of the tracking process

The first term in Eq.(19) is just $E_{I_t}^{(m,n)}$ calculated using Eq.(18) by considering the pixels only in the region. The second term in Eq.(19) ensures that each estimated intensity $a_t^{(k_h)}$ will agree with its predicted value $\widetilde{a}_t^{(k_h)}$ to some degree controlled by λ_a. Eq.(20) ensures that each estimated position $(x_t^{(k_h)}, y_t^{(k_h)})$ is within a circle centered at its predicted position $(\widetilde{x}_t^{(k_h)}, \widetilde{y}_t^{(k_h)})$ with radius $\triangle$.

3.4 The Tracking Process

The tracking process is illustrated in Fig. 3. After the initial detection result is obtained by processing all the images, the tracking module starts. Once it is finished, the order of the image sequence is reversed and the tracking module performs again to provide the final result. As the reader may notice, splitting-hypothesis is not mentioned in section 3.3. However, by tracking in the backward time direction, the problem can be solved, because a splitting event in the forward timeline is equivalent to a merging event in the reversed timeline.

3.5 Evaluation on Synthetic Data

Synthetic datasets are created with different signal to noise ratios (SNRs) and particle densities. A set of CCP trajectories are obtained from real data, and are adjusted by smoothing and rescaling their intensity-time curves. Each simulated trajectory can be generated by randomly sampling from that dataset and randomly putting to image plane. After the clean images are obtained, each image is convolved with point spread function, and then noises are added. Two types of noises are considered in simulation: the Poisson (shot) noise of input photon and the excess noise generated in the EMCCD. The SNR of each dataset is defined as the average SNR of individual particles. By varying the background noise level, the SNR of each dataset can be tuned in a large range. We choose two particle densities: $0.005/\text{pixel}^2$ and $0.008/\text{pixel}^2$ to represent the densities of different regions.

To measure tracking performance, Jaccard similarity is calculated for the tracking result on each dataset, given by

$$J = \frac{TP}{TP + FN + FP} \tag{21}$$

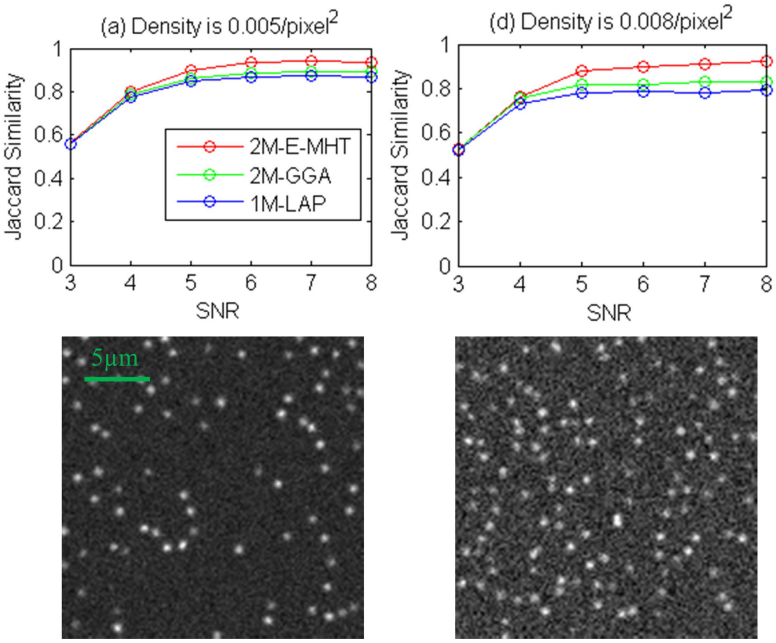

Fig. 4. Top Row: the Jaccard similarity scores of the three methods in different scenarios. Botom Row: Tow synthetic image samples (128x128 pixel, and 1 pixel=180nm): (a) Density=0.005/pixel^2 and SNR=8. (b) Density=0.008/pixel^2 and SNR=5.

True (false) positive TP (FP) is the total number of correct (wrong) associations in the recovered trajectories, and false negative FN is the sum of the lifetimes of the ground truth trajectories minus the true positive. Before the calculations, the best match between the recovered trajectories and the ground truth trajectories is found. The distance threshold is set to be 3 (pixel), which means if the distance between two positions in two trajectories is greater than the threshold, then the two positions do not match to each other, i.e., a wrong association occurs.

To evaluate the proposed method, we may compare it to some particle tracking methods in the literature. However, since different parameters and detection methods are used for different applications, direct comparisons are very difficult and unfair. Instead, we choose two representative methods modified from two general particle tracking methods. The first method uses Brownian motion model and linear assignment programing (LAP), which is based on the method in [4]. We name the first method as 1M-LAP where M means model. The second method uses the two models with IMM filter described in section 3.1 and global greedy assignment (GGA), which is based on the method in [3]. We name the second method as 2M-GGA. Both of the two methods use the same detection module described in section 3.2. We name our proposed method as 2M-E-MHT where E means extended.

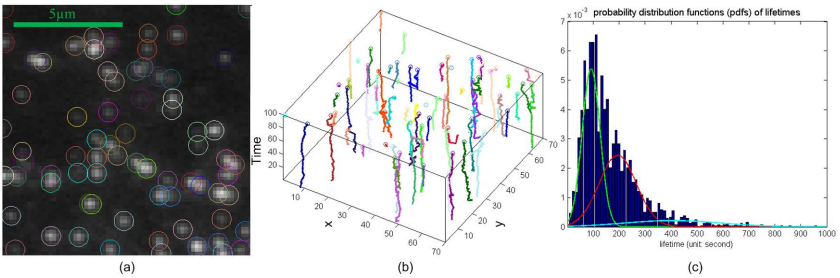

Fig. 5. (a) A sample image with circles indicating detected particles. (b) Sample trajectories over time (vertical axis), uint in x-y plane is pixel. (c) Lifetime distributions.

The performance scores are shown in Fig. 4. The method 1M-LAP has the lowest performance because it uses the least amount of information. By using better models, the method 2M-GGA does better than the method 1M-LAP in some scenarios. By applying the extended MHT framework with the CCP models, the proposed method 2M-E-MHT performs consistently better than the other two methods when SNR is greater than 4.

3.6 Evaluation on Real Data

Wild type mouse fibroblasts were transiently transfected with GFP tagged μ2 subunit of Adaptor Protein 2 complex by electroporation, and were immediately plated at subconfluent densities ontofibronectin-coated 35mm glass bottom culture dishes (MatTek, Ashland, MA, USA) for 24 hours. Images were acquired using a Nikon TiEinverted microscope equipped with 100× oil objective lens (1.49-NA). Excitation light was provided by 488nm diode-pumped solid-state lasers coupled to the TIRF illuminator through an optical fiber. The output from the lasers was controlled by an acousto-optic tunable filter, and fluorescence signal was acquired with an EM-CCD camera (DU-887; Andor).

Examples of detected particles and the trajectories are shown in Fig. 5(a) and (b), respectively. The lifetime histogram is shown in Fig. 5(c). Mixture Gaussian distribution functions are fitted to the normalized histograms, and three populations are indentified. Other analysis can be performed based on tracking result, and details are omitted due to space limit.

4 Extension for Cell Segmentation

The method can be extended for 3D tracking in other applications by extending the detection method to 3D and using relevant state models. Here, we show that the method can be indeed extended for 3D cell segmentation.

Stem cells play a key role in hair regeneration [17], however, the underlying mechanisms still remain unclear. For this research, we have acquired cell images in the epidermis by using two-photon excitation microscopy which can penetrate

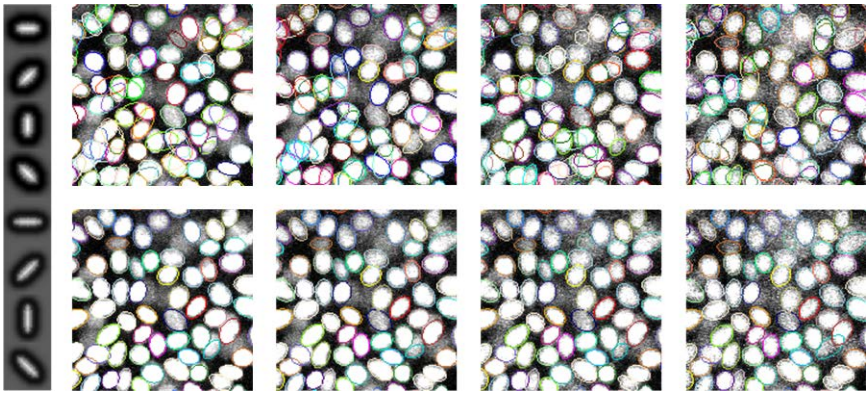

Fig. 6. Leftmost: Samples of the ellipse-shaped filters. Top row: Cell observation hypotheses over 4 successive z-steps. Bottom row: The selected cell observations.

deep tissues. By considering the z-slices as time frames, segmentation in 3D just becomes tracking in 2D+t. Each cell is just a 'big particle'. The strategy of hypothesis generation is similar to that described in section 3.3. For each pixel location on each z-slice image, we apply ellipse-shaped filters with different sizes and orientations as shown in Fig.6, and select the best ellipse that has the highest filter output. Therefore, multiple cell observation hypotheses are generated for each image as shown in Fig.6. To calculate energies related to observation hypotheses, we set λ_a in Eq.(19) as zero, and set $\log p\left(\mathbf{I}_{(t,\Omega_m)} \middle| \mathbf{D}^{(m,n)}_{(t,\Omega_m)}\right)$ to be equal to the sum of the corresponding filter outputs. To link the cell observations in 2D images, the same four types of "trajectory" hypotheses are used, and we only use the second model described in section 3.1. After applying integer programming, the best set of hypotheses are selected as shown in Fig.6.

This method is full automatic and works for crowded cells because of the advantage of the filter based approach, and is relatively easy to be implemented. Since cells can be generally represented by ellipses, the method can serve as an automatic initial segmentation method.

5 Conclusions

We have proposed a tracking method and applied it for clathrin mediated endocytosis analysis, and shown the extension for cell segmentation. The original MHT framework is extended by considering more types of hypotheses, and the related optimization problem is solved using integer programming. For CCP tracking, special strategies are designed for multiple hypothesis generation. The tracking method has been demonstrated on synthetic data and real data. By considering the z-slices as time frames, the method can be extended for 3D cell segmentation. The method is currently being used to investigate the mechanisms of clathrin mediated endocytosis, and we will expect more applications.

References

1. Slepnev, V.I., Camilli, P.D.: Accessory factors in clathrin-dependent synaptic vesicle endocytosis. Nature Reviews Neuroscience 1, 161–172 (2000)
2. Brandenburg, B., Zhuang, X.: Virus trafficking – learning from single-virus tracking. Nature Reviews Microbiology 5, 197–208 (2007)
3. Genovesio, A., Liedl, T., Emiliani, V., Parak, W.J., Coppey-Moisan, M., Olivo-Marin, J.-C.: Multiple particle tracking in 3-d+t microscopy: method and application to the tracking of endocytosed quantum dots. IEEE Transactions on Image Processing 15(5), 1062–1070 (2006)
4. Jaqaman, K., Loerke, D., Mettlen, M., Kuwata, H., Grinstein, S., Schmid, S.L., Danuser, G.: Robust single-particle tracking in live-cell time-lapse sequences. Nature Methods 5, 695–702 (2008)
5. Carter, B.C., Shubeita, G.T., Gross, S.P.: Tracking single-particles: a user-friendly quantitative evaluation. Physical Biology 2(1), 60–72 (2005)
6. Smal, I., Draegestein, K., Galjart, N., Niessen, W.J., Meijering, E.H.W.: Particle filtering for multiple object tracking in dynamic fluorescence microscopy images: Application to microtubule growth analysis. IEEE Transactions on Medical Imaging 27(6), 789–804 (2008)
7. Reid, D.B.: An algorithm for tracking multiple targets. IEEE Transactions on Automatic Control 24, 843–854 (1979)
8. Chenouard, N., Bloch, I., Olivo-Marin, J.-C.: Multiple hypothesis tracking in microscopy images. In: IEEE International Symposium on Biomedical Imaging: From Nano to Macro, pp. 1346–1349 (2009)
9. Feng, L., Xu, Y., Yang, Y., Zheng, X.: Multiple dense particle tracking in fluorescence microscopy images based on multidimensional assignment. Journal of Structural Biology 173, 219–228 (2011)
10. Poore, A.B.: Some assignment problems arising from multiple target tracking. Mathematical and Computer Modelling 43, 1074–1091 (2006)
11. Genovesio, A., Olivo-Marin, J.-C.: Split and merge data association filter for dense multi-target tracking, pp. 677–680 (2004)
12. Thomann, D., Rines, D.R., Sorger, P.K., Danuser, G.: Automatic fluorescent tag detection in 3d with super-resolution: application to the analysis of chromosome movement. Journal of Microscopy 208(1), 49–64 (2002)
13. Liang, L., Shen, H., De Camilli, P., Toomre, D.K., Duncan, J.S.: An expectation maximization based method for subcellular particle tracking using multi-angle TIRF microscopy. In: Fichtinger, G., Martel, A., Peters, T. (eds.) MICCAI 2011, Part I. LNCS, vol. 6891, pp. 629–636. Springer, Heidelberg (2011)
14. Li, X.R., Jilkov, V.P.: Survey of maneuvering target tracking. Part v. Multiple-model methods. IEEE Transactions on Aerospace and Electronic Systems 41(4), 1255–1321 (2005)
15. Robbins, M.S., Hadwen, B.J.: The noise performance of electron multiplying charge-coupled devices. IEEE Transactions on Electron Devices 50(5), 1227–1232 (2003)
16. Liang, L., Xu, Y., Shen, H., Camilli, P.D., Toomre, D., Duncan, J.S.: Automatic detection of subcellular particles in fluorescence microscopy via feature clustering and bayesian analysis. In: IEEE Workshop on Mathematical Methods in Biomedical Image Analysis, pp. 161–166 (2012)
17. Rompolas, P., Deschene, E.R., Zito, G., Gonzalez, D.G., Saotome, I., Haberman, A.M., Greco, V.: Live imaging of stem cell and progeny behaviour in physiological hair-follicle regeneration. Nature (2012)